Detection and Classification of Holes in Point Clouds

Nader H. Aldeeb and Olaf Hellwich
Computer Vision and Remote Sensing, Technische Universität Berlin, Berlin, Germany
nader.h.aldeeb@gmail.com, olaf.hellwich@tu-berlin.de

Keywords: Point Cloud, Hole Detection, Hole Classification, Hole Filling, Surface Reconstruction, Textureless Surfaces, Segmentation with Graph Cuts.

Abstract: Structure from Motion (SfM) is the most popular technique behind 3D image reconstruction. It is mainly based on matching features between multiple views of the target object. Therefore, it gives good results only if the target object has enough texture on its surface. If not, virtual holes are caused in the estimated models. But, not all holes that appear in the estimated model are virtual, i.e. correspond to a failure of the reconstruction. There could be a real physical hole in the structure of the target object being reconstructed. This presents ambiguity when applying a hole-filling algorithm. That is, which hole should be filled and which must be left as it is. In this paper, we first propose a simple approach for the detection of holes in point sets. Then we investigate two different measures for automatic classification of these detected holes in point sets. According to our knowledge, hole-classification has not been addressed beforehand. Experiments showed that all holes in 3D models are accurately identified and classified.

1 INTRODUCTION

Generating accurate 3D image reconstruction has found its application in a wide variety of fields, such as computer aided geometric design, computer graphics, virtual reality, computer vision, medical imaging, human computer interaction, computer animation, and robotics. Because of the availability of relatively cheap sensors, surface reconstruction has gained considerable interest (Zaman et al., 2016). Nowadays, many simple applications that are based on Structure from Motion (SfM) allow users to create own high-quality 3D models on their smart-phones not requiring any experience or specific knowledge regarding that technique (Muratov et al., 2016). SfM is based on matching correspondences between multiple views of the target object. That matching is based on correspondence establishing of features such as corner points (edges with gradients in multiple directions) from one image to the other. Therefore, feature detection is highly needed in SfM. One of the most widely used feature detectors is the Scale-Invariant Feature Transform (SIFT) (Lindeberg, 2012). Unfortunately, the performance of the SIFT algorithm over texture-less surfaces is poor, because no feature point can be detected in such surfaces (Alismail et al., 2016). Consequently, SfM technique fails to estimate 3D information in regions having weak texture information, where no matching points can be found (Saponaro et al., 2014). That is the reason why most of the popular 3D reconstruction techniques give good results only if the target object has enough texture on its surface. If not, virtual holes appear in the estimated models. For this kind of low-textured objects, laser scanners are frequently used instead of the traditional image based 3D reconstruction techniques. But, holes may also appear in the resulting models due to surface reflectance, occlusions, and accessibility limitations (Wang et al., 2007).

These days, having a high-quality reconstruction of objects is an essential demand by many applications. Therefore, hole-filling or surface completion has become an important component in 3D image reconstruction process. But, no hole filling can be applied without the detection of holes in point clouds. So, hole-detection in point sets is also an important component in that process. Usually, 3D image reconstruction methods produce unstructured point clouds. That is, there is no explicit connectivity information encoding the surface of the object. This makes the problem of the detection of holes on the surface an ill-defined problem (Bendels et al, 2006).

It is worth mentioning that not all holes appearing in the estimated model are virtual, i.e. due to missing reconstructions of featureless surfaces.

Aldeeb N. and Hellwich O.
Detection and Classification of Holes in Point Clouds.
DOI: 10.5220/0006296503210330
In *Proceedings of the 12th International Joint Conference on Computer Vision, Imaging and Computer Graphics Theory and Applications (VISIGRAPP 2017)*, pages 321-330
ISBN: 978-989-758-227-1

Some of the holes may also represent a real physical hole, which is part of the structure of the object being reconstructed. Unfortunately, just looking at the point cloud, it is almost impossible to differentiate between these two types of holes (real and virtual). Particularly, when there is a real physical hole in the structure of the target object having uniformly distributed inner-color or inner-details not appearing in the 2D views, this kind of regions will appear as regions missing depths in the estimated model. These are real holes that should be left as they are during the filling process.

The ambiguity in differentiating between real and virtual holes is a significant problem, which is usually faced when running a hole-filling algorithm. Thus, analysing each of the detected holes and classifying them to either real or virtual hole is a very important component in hole-filling process.

Finally, it is now clear that the problem of hole-filling in point clouds requires two tasks. First, identifying the holes, and then classifying them. By classification, the necessity of filling the identified hole can be determined. Unfortunately, both tasks are nontrivial. But in this paper, we propose a simple approach which will contribute to the accurate detection and classification of holes in point clouds, and consequently support systems for surface reconstruction and hole filling.

The rest of this paper is organized as follows: section 2 presents a brief background and lists the related work. Section 3 discusses the proposed approach. Experimental results and discussion can be found in section 4. Finally, section 5 concludes with a conclusion, perspectives, and future work.

2 BACKGROUND AND RELATED WORK

Structure from Motion (SfM) techniques have attracted researchers since the work of (Tomasi and Kanade, 1992). SfM algorithm involves finding correspondences between different input images for the object being reconstructed, and then estimates a 3D model and a set of camera parameters. Therefore, reconstructing regions having low textures is challenging for most of SfM-based approaches.

As mentioned before, the need for accurate 3D models makes hole-filling a very important problem. For a successful hole-filling, accurate detection and classification of holes in point clouds are needed. According to our knowledge, and after an intensive review of the literature, not much work has been published about detecting holes in point clouds. Nevertheless, some methods employed either special equipment or triangular meshes, sometimes associated with some input entered manually by users for hole-identification. For example, in (Noble et al., 1998), the internal geometry feature of 3D objects is measured by employing an X-ray inspection method; thereby they were able to position the drilled holes on the object's surface. In (Kong et al., 2010), a hole-boundary identification algorithm for 3D closed triangle mesh is presented. In this method, the user has to interactively select the region of interest by mouse dragging. From our point of view, this method has one more drawback besides the need for manual inputs. Dependence on meshes instead of point clouds will not guarantee the detection of all holes, because some meshing algorithms may fill the regions of missing depth. Consequently, this prevents distinguishing real from virtual holes.

The authors of (Wang et al., 2012) proposed a method which aims to find solid holes inside 3D models. This method is also based on triangular mesh models. By grouping interconnected coplanar triangles, they extract the contour of the model using the boundaries of the adjacent planes. Then, based on the extracted contour, they form several disjoint clusters of model vertices. Finally, by analysing the relationship between the clusters and planes, holes are identified. But, this method only finds solid holes inside models, and does not detect regions of missing depths.

The main goal of (Wang et al., 2007) is filling holes in locally smooth surfaces. But, as a pre-processing step, holes are found based on the triangular mesh of the input point cloud. In this method, holes are identified automatically by tracking boundary edges. If an edge belongs only to a single triangle, then it is a boundary edge, otherwise it is a shared edge, which shares more than one triangle. But, employing this strategy in finding holes will detect all holes including the real holes those need not be filled. Therefore, in this work, user input is required as an assistance. So, again, manual user inputs are needed in this work.

An automatic hole-detection approach has been presented in (Bendels et al., 2006). Properties of point sets have been investigated to derive several criteria which are then combined into an integrated boundary probability for each point. This method seems to be robust, but we have noticed that it has some drawbacks. First, in their combination of probability criteria, they used some weights, which have to be set by the user according to visual inspection. Second, they have a set of predefined parameters, which limits the scalability of the approach. For example, a predefined diameter is set for the hole to be detected.

Some other approaches address a closely related problem. For example, (Dey and Giesen, 2003) present an approach for the detection of under-sampled regions. The detection is guided using a sampling requirement, which has been defined to ensure a correct reconstruction of surfaces. For example, for correct reconstruction, every point on the surface should have at least one sample point within a ball with a predefined size. But, according to this definition, their method will not succeed in detecting holes in planar regions, where this requirement is mostly fulfilled by a little number of samples.

3 THE PROPOSED ALGORITHM

Fig. 1 shows the flowchart of the proposed algorithm. In the following subsections, each of the main processes will be discussed in brief using demonstration examples.

3.1 Input a Number of Views

The first step in the proposed algorithm requires a number of input images. Because the technique proposed in this paper uses stereo correspondences, two calibrated images from different viewpoints for the object being reconstructed are needed at least.

3.2 Bundle Adjustment

Bundle Adjustment is the process of jointly refining a set of initial camera and structure parameter estimates for finding the set of parameters, which most accurately predict the locations of the observed points in the set of available images (Alismail et al., 2016). Assuming we have n 3D points that are seen in m views, and the projection of the i^{th} point into view j is denoted by X_{ij}, and let v_{ij} be a binary number equals 1 if the point i is visible in view j and 0 otherwise. Also, let a_j denote the vector carrying the parameters of camera j and b_i is the vector carrying the coordinates of the 3D point i. Then by minimizing the following energy function, we get the optimal projection matrix for each camera.

$$\min_{a_j, b_i} \sum_{i=1}^{n} \sum_{j=1}^{m} v_{ij} d\left(Q\left(a_j, b_i\right), X_{ij}\right)^2 \quad (1)$$

where, $Q(a_j,b_i)$ denotes the predicted projection of point i onto view j and $d(x,y)$ denotes the Euclidean distance between the image points x and y. In our research, we used Bundler (Snavely et al., 2008; Snavely et al., 2006) for getting the camera matrices.

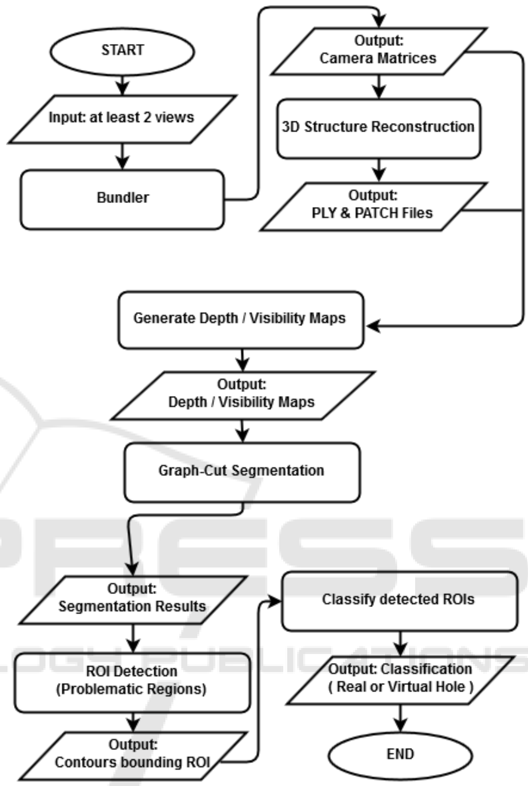

Figure 1: Flowchart of the proposed approach, detection and classification of holes in point clouds.

3.3 Reconstruction of the 3D Structure

Patch-based Multi-View Stereo (PMVS) software (Furukawa and Ponce, 2010) has been employed to reconstruct the 3D structure of objects visible in images. According to our proposed approach, we need to know the views in which the generated 3D points are visible. One of the outputs generated by PMVS is the PATCH file, which contains full reconstruction information. That includes the number of reconstructed 3D points, the 3D location, the normal, and photometric consistency score for each point. Also, it states the number of images in which the point is visible as well as the actual image indexes. That is the main reason for using PMVS in our implementation.

3.4 Generating Depth and Visibility Maps

The goal of this research is to analyse the 3D structure of objects appearing in images through investigating the combination of the 3D structure together with the features and details provided by the images. Therefore, the goal of this process is to relate the 3D information, which we got in the previous process, with the 2D views (images).

In point clouds, each point can be denoted using a homogeneous 3D coordinate as (*x y z 1*). Similarly, the homogeneous 2D coordinate of its projection into images can be denoted as (*u v 1*). From the patch file, we know the view in which each of the 3D points is visible. Then, using the corresponding camera matrix, *P*, we can relate each 3D-coordinate to its 2D-coordinate by following (2), where *d* is the depth of that point.

$$d[u\ v\ 1]^T = P[x\ y\ z\ 1]^T \tag{2}$$

We can thus generate depth-maps for our object based on all its views (images). Because images are 10 times down sampled, the value of each pixel in that map is the average of the depth values of the projected 3D points into that pixel location. If for a given pixel no depth information is given, it is assigned a depth equals $\sqrt{2}$ times the maximum depth in the map (very far). Thereby, we guarantee that the generated value is larger than the maximum depth in the map. Here, it is worth mentioning that values other than $\sqrt{2}$ can also be used. But the used value has a direct effect in segmentation, as it will become clear in section 3.5.2.

Also, exploiting the visibility information from the PMVS's PATCH file, we can generate visibility-maps, where each pixel is assigned a number which equals the total number of 3D points which are projected to that pixel location. This happens because of the down sampling of images. Fig. 2 shows both maps for one view of the house model as an example (see section 4 for more details about the dataset). In the visibility-map, for demonstration, a pixel is marked red if it has depth information in the generated 3D structure and marked black otherwise.

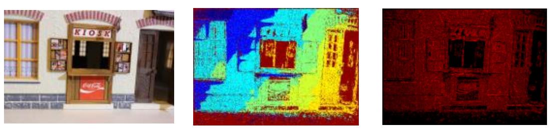

(a) (b) (c)

Figure 2: Example depicting (a) original image, (b) depth-map and (c) visibility-map.

Afterwards, we will use either of these maps to identify the problematic regions, which have no depth information, out of each image employing graph cuts.

3.5 Segmentation using Graph Cuts

To take advantage of the competent solutions of graph-based approaches for segmentation problems, we built an s-t-graph (Boykov and Funka-Lea, 2006). The number of nodes in the graph equals to the number of pixels in the input map. Two more additional nodes, the source and the sink, represent the segmentation labels. Each node in the graph is connected to its 8-neighborhood nodes based on the neighbourhood information of pixels. In addition, each node is joined to the source and the sink using two weights, which represents the likelihood of the corresponding pixel to either of the segmentations labels. Fig. 3 shows a sketch of the graph. For accurate segmentation results, weights form different types of regions must assure a large difference. For reasons of comparison, weights are selected based on the depth-maps one time and on the visibility-maps at the other time.

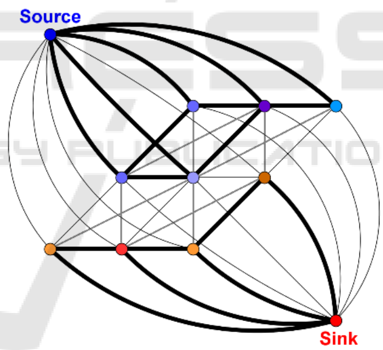

Figure 3: Sketch of the graph and connectivity (w3.impa.br/~faprada).

3.5.1 Supporting Graph Cut Segmentation

For supporting our graph-based segmentation, before we set the weights for the graph, we estimate another kind of segmentation, which gives an indirect indication about the nature of pixels. That is, whether they have depth information or not. Since SfM techniques perform poorly in regions having weak or no textures, we first detect these regions in original images, then each pixel is classified to belong either to a textured or texture-less region. Finally, weights on graph edges are affected by those classification results.

According to (Scharstein and Szeliski, 2002), texture-less regions are defined as regions where the average of the squared horizontal gradient over a predefined window is below some given threshold. Using (3), we get the squared horizontal intensity gradient for two neighbouring pixels. It is calculated over the three color-channels, c, and then averaged. If we repeat this for all pixels in image, we get the Gradient Image *GI*, where *i* and *j* are the image's row and column indices respectively.

$$GI(i,j+1) = \frac{1}{3}\sum_{c=1}^{3}(I_c(i,j) - I_c(i,j+1))^2 \qquad (3)$$

If for a given region, which is covered by a window of a predefined size $S \times S$, the average of the squared gradient is less than some predefined threshold T, then this region is assumed as a texture-less region. The average squared gradient over a predefined window can be calculated as:

$$Avg = \frac{1}{S^2}\sum_{a=-S/2}^{S/2}\sum_{b=-S/2}^{S/2} GI\,(i+a, j+b) \qquad (4)$$

Image indices *i* and *j* are set such that the window remains inside the image boundaries each time the *Avg* is calculated. Pixels falling in weak or texture-less regions are assigned the value $\beta = 1$, (white color). All other pixels are assigned the value $\beta = 0$, (black color). Fig. 4 shows the classification results for one view of the Folder model (see section 4 for more details about the dataset). We used the parameters $S=9$ and $T=3$.

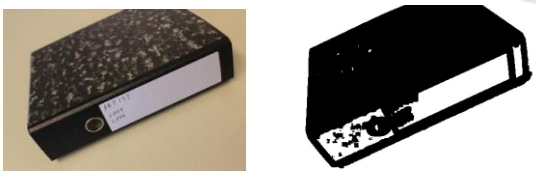

(a) (b)

Figure 4: Example showing (a) original image, (b) "textured", 'texture-less" classification results.

3.5.2 Segmentation based on Depth-Maps

Based on depth-maps, the weights of the graph are given in a way such that the min-cut / max-flow goes through regions where no depth information is available. If the maximum depth for a given depth-map, D, is D_{max}, and the depth for a given point, p, is $D(p)$, the term weight, W_p, is estimated using (5). Where, β_p is the supporting parameter, which is the classification of the pixel corresponds to point p (see section 3.5.1). And α is a tuning parameter, used to suppress the effect of the supporting term. This kind of suppression is very important, because the presence of a pixel in a textured region, $\beta_p = 0$, does not guarantee that we have a corresponding depth information. This usually happens if the pixel is not visible in other views. Therefore, we set α to 10, this has the effect of a little decrease in point weight. It is worth mentioning that if a pixel falls in a texture-less region, $\beta_p = 1$, then the supporting term becomes zero. So, the maximum possible point weight is guaranteed. This makes sense, as there will be no corresponding depth information for that pixel. Basically, W_p is the probability that point p belongs to a problematic region.

$$W_p = \frac{D(p)}{\sqrt{2} * D_{max}} - \underbrace{(1-\beta_p) * \frac{\log_{10}\sqrt{2}}{\alpha}}_{\text{supporting term}} \qquad (5)$$

In addition, each edge, E_{pq}, which connects any two points, p and q, is assigned two weights, W_{pq} and W_{qp}, as seen in (6) and (7) respectively.

$$W_{pq} = W_p \qquad (6)$$

$$W_{qp} = \begin{cases} W_q, & 1 - W_p \geq W_q \\ 1 - W_p, & otherwise \end{cases} \qquad (7)$$

Fig. 5 (b) shows the result of segmenting a depth-map, which has been shown in Fig. 2 (b). White color is used to refer to pixels having no depth information.

3.5.3 Segmentation based on Visibility-maps

As in section 3.5.2, the weights of the graph are given such that the min-cut / max-flow goes through the problematic regions, but now based on the visibility-maps. Based on our definition of a visibility-map, *V*, problematic regions are the regions composed of pixels that have the least number of projections. Therefore, these points are given highest weight in the graph. For some given point, p, which has the total number of projections $V(p)$, the term weight, W_p, is estimated as in (8). Note that here we also use a supporting term, which is exactly same as the term used in section 3.5.2.

$$W_p = \left(1 - \min\left(1, \frac{V(p)}{2}\right)\right) - (1-\beta_p) * \frac{\log_{10}\sqrt{2}}{\alpha} \qquad (8)$$

Also, each edge, E_{pq}, is assigned two weights, W_{pq} and W_{qp}, which are calculated as in section 3.5.2 but now point weights are estimated using (8). Fig. 5 (c) shows the result of segmenting a visibility-map, which has been shown in Fig. 2 (c). White color is used to refer to pixels having no depth information.

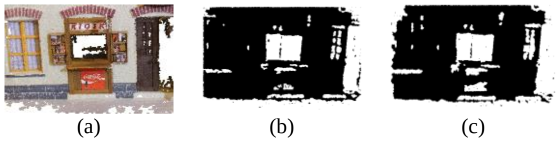

Figure 5: Segmentation results for both maps shown in Fig 2. Part (a) is the original point cloud, (b) depth-map segmentation, and (c) visibility-map segmentation.

At first glance, segmentation results look in somehow the same and this might also be supported theoretically. Because if we have a 3D point, this means for sure that it is visible in at least two of the views, so depth means visible. But, for the detection of the problematic regions, we prefer depending on depth-map-based segmentations for the following reason: Taking the exact depth value of each point for weighting the graph is more efficient and robust than taking the cue that the point is visible in the view. Because, the noisy 3D points will be noted as visible in views, and will contribute in weight estimations with the same amount as the non-noisy points. But based on depth-maps, noisy points, which have been assigned erroneous depths, will contribute with their depths, which will be different from the other non-noisy points depths.

3.6 Regions of Interest (ROI) Detection

In this process, we need not only delineate the problematic regions, but also, we need a direct access to the points inside those regions for further processing. Therefore, contours will be the most appropriate tool fulfilling our demand. We also need the detected contours to be closed. I.e., the boundaries or edges of the problematic regions need to be connected. In the segmentation results, which we already saw in Fig. 5, the problematic regions, those having no depth information, are tightly delineated or connected. So the detection of such regions using closed contours is quite easy. But, after many observations, we have noticed that this might not be the case all the time. This presents challenges in the detection process. Therefore, as an attempt to connect the non-connected edges, we decided to first detect the edges of the object being reconstructed using the original images, and then combine the detected edges with the segmentation results. Fig. 6 shows an example, where this combination helps in detecting closed contours surrounding ROI. As shown in (d), it is clear that the contours are not tightly delineating the problematic regions. But after the inclusion of the object's detected edges to the segmentation edges, as shown in (e), the detected contours are now delineating the problematic regions in a helpful manner, as seen in part (f).

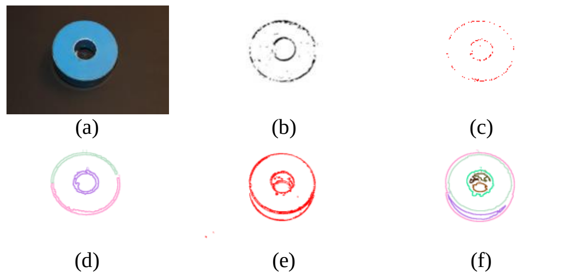

Figure 6: Example depicting the benefit of combining both depth and real edges in the process of ROI detection. (a) Original Image. (b) depth-map segmentation. (c) Detected edges based on (b). (d) Detection of the ROI based on (c). (e) Combining both the original object edges with the depth based edges shown in (c). (f) Detection of the ROI based on (e).

3.7 Classification of the Detected Problematic Regions

After the detection of the problematic regions in images, simple approaches are investigated to check their performance in the classification of the detected regions.

First, we conduct a statistical measure on the pixels in each problematic region to be classified. This measure assumes that the behaviour of each ROI among the views should tell about the nature of it. This assumption has been inspired from the fact that the human does the same whenever holes are to be recognized by looking for details inside the hole, like the shadow. For the sake of robustness, the calculations are done using Hue-Saturation-Value (HSV) color-space. Because, HSV separates the image intensity from the color information (Haluška et al., 2015). For the classification of a given detected problematic region P, which appears in n views, we first find the mean set, $M = \{\mu_1, \mu_2, .., \mu_n\}$, where μ_i is the average intensity inside the region P in view i. Then we find the variance and standard deviation of the set M as $\sigma^2 = (1/n)\sum_{i=1}^{n}(\mu_i - \mu)^2$, and $\sigma = \sqrt{\sigma^2}$ respectively, where μ is the mean of the set M. Finally, we make a list of pixels appearing inside the problematic region P in all the views and check each pixel p whether it satisfies the condition $(\mu - \lfloor\sigma\rceil) \leq p \leq (\mu + \lfloor\sigma\rceil)$ or not. If the percentage of pixels satisfying that condition exceeds a given threshold, T (see section 4), then P is assumed as a virtual hole, otherwise it is assumed as a real hole.

Second, we experiment a depth measure, which re-projects the problematic region to be classified into the 3D space and simply differentiates the average depth of the 3D points on the contour delineating the region from that inside the same region. If the region corresponds to a real physical hole, then it is supposed to have a significant depth difference. Otherwise, if the region corresponds to a virtual hole, the difference is supposed to be negligible. A depth threshold, T_d, is used for that reason (see section 4).

4 EXPERIMENTAL RESULTS

As mentioned before, hole-classification has not been addressed beforehand. Therefore, no comparisons to other works will be given in this section. However, many experiments have been conducted to investigate the performance of the proposed approach in terms of accuracy in detecting and classifying holes. The material used in this part includes a dataset of 55 models for different indoor objects and scenes, each of which is reconstructed using VisualSFM (Wu, 2011) based on a set of images (5184 x 3456) taken from different viewpoints. For performance issues, after estimating the 3D models, all images are 10 times down sampled. Fig. 7 shows a sample set of the models used in this paper.

The reconstructed models contain many problematic regions, with size ranges from 600 to 150,000 pixels. The size of a problematic region P is the least number of pixels appear in P when projected to each of the down-sampled views. As a ground truth, we make a record of randomly selected set of problematic regions, each of which is assigned to either real or virtual hole. 40% of the selected set are for real holes and 60% are for virtual holes.

Training our statistical and depth classifiers is to estimate the values of thresholds, T and T_d, by which problematic regions can be classified. For that reason, 20 models are selected randomly for training. Many observations have been applied for different values of these thresholds. The accuracy corresponds to each observation has been recorded. The highest average classification accuracy was obtained when setting T = 30 % and T_d = 0.01 (normalized).

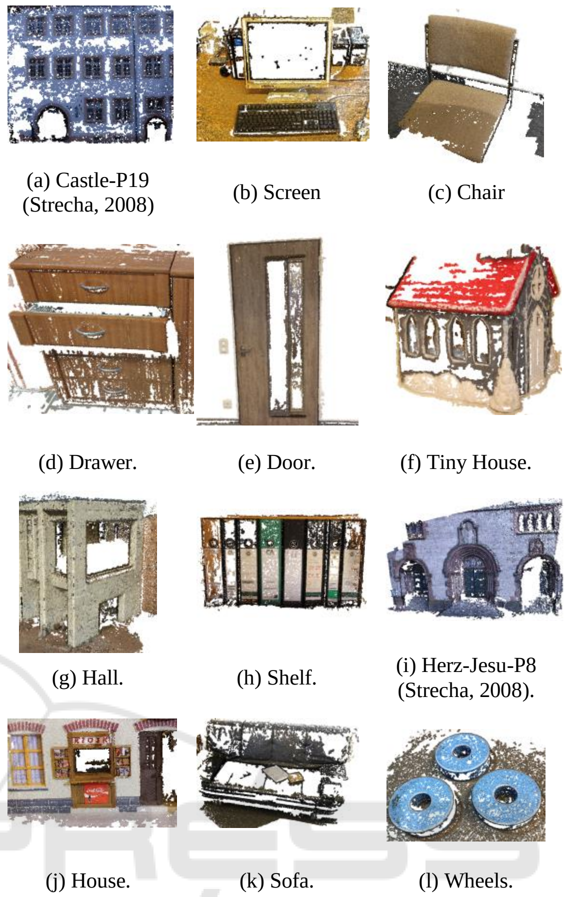

Figure 7: Some of the models used in evaluating the proposed approach.

4.1 Evaluating the Detection of the Problematic Regions

Figure 8 shows an example of problematic regions detection. As mentioned before, contours are used to delineate the problematic regions. Therefore, to quantitatively assess the detection accuracy, we measured the similarity between the detected contour and the ideal contour, which is set manually. This has been done for a set of the test models. The similarity between contours is measured using the Pratt's Figure of Merit (PFOM) (Abdou and Pratt, 1979) defined in (9). This measure basically depends on estimating the distance between point pairs of the two contours.

$$R = \frac{1}{max(I_I, I_D)} \sum_{i=1}^{I_D} \frac{1}{1 + \alpha {d_i}^2} \quad (9)$$

Where, I_I and I_D are the numbers of edge points in the ideal, ground truth, and the detected contour respectively. d_i is the distance between the i_{th} pixel in the detected contour and the nearest pixel in the ideal contour. Finally, α is an experimental constant which was set to *1/9* according to (Abdou and Pratt, 1979). The value of R ranges between *0* and *1*. The larger the value of R, the more accurate the detected contour is. The average value of R we got in this experiment is 0.89. This value means that approximately 90% of the ROI is detected. This is sufficient for the next processing steps to achieve the goal of this research. This is because 90% of the region's area will definitely contain most of the details, in which we are interested for the next processing step.

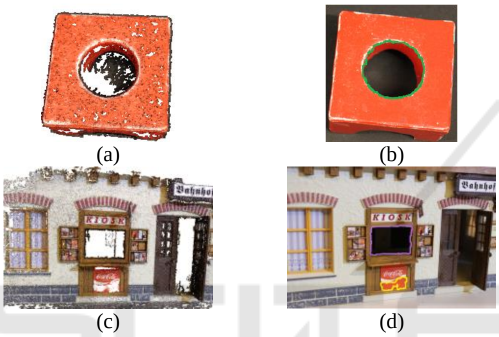

Figure 8: Demonstrating the detection of the problematic regions. (a) Toy Model, reconstructed using Visual-SFM (10 images). (b) detected problematic region in one of the images used in (a). (c) House Model, reconstructed using Visual-SFM (10 images). (d) Two detected problematic regions in one of the images used in (c).

4.2 Evaluating the Classification of the Problematic Regions

To evaluate the accuracy of the proposed classification approaches mentioned in section 3.7, we compare the outcome of the classification experiments with the ground truth classification. The average accuracies for classifying virtual and real holes using the proposed statistical classifier can be seen in Fig. 9. Problematic regions are categorized into 6 categories based on their sizes.

The average true positive rates for classifying virtual and real holes are 81.74% and 80.09% respectively. As seen in Fig. 8, the smaller the problematic region is, the lower the true positive rate we get. Many small virtual holes were classified as real holes. The reason behind this is the effect of the change in lighting conditions on those regions from one view to the other. This effect usually biases our classifier. Also, many small real holes were classified as virtual holes. Because the details behind these holes are not clearly visible.

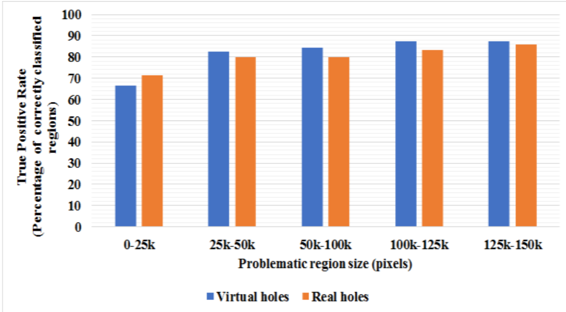

Figure 9: True positive rates for the statistical classifier.

Figure 10 shows the average accuracies for classifying virtual and real holes using the proposed depth classifier. The average true positive rates for classifying virtual and real holes are 80.44% and 83.76% respectively. In fact, for the latest measure, the models, in which problematic regions were false positive or false negative, are either noisy models or having regions, in which it is very difficult to calculate the measure because of having no depth information inside it.

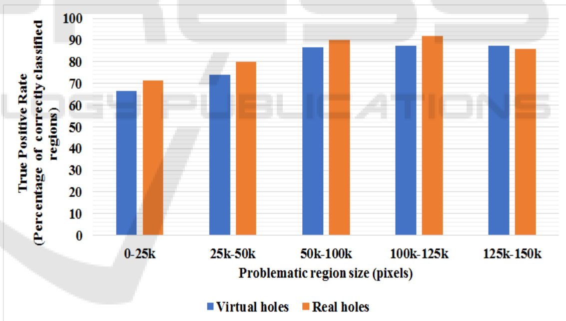

Figure 10: True positive rates for the depth classifier.

4.3 Evaluating the Efficiency of the Proposed Approach

The results listed in this section were taken using a personal computer running Windows 7 64-bit operating system with Intel Core i7 3.6 GHz processor and 16 GB Memory installed. The approach has been implemented using C++.

The efficiency of the proposed approach is highly dependent on the starting point from which the processing will start, see Fig. 1. The point from which we start usually depends on which type of data do we have. If we only have the images of the object and still have no 3D reconstruction of it, then the time consumed by the proposed approach will include the time for the bundler and 3D reconstruction pipeline. Unfortunately, these two components usually take long time, depending on the size and number of input images (approximately 3 minutes to process 8 images each of which has size 5184×3456). Nonetheless, the rest of components in the proposed approach are very efficient. Fig. 11 shows the average time required for generating and segmenting depth-maps given different numbers of input images. It is worth mentioning that, as the number of the input images increases, the classifications of the problematic regions will become more stable. But, as seen in the figure, the larger the number of views results in longer processing times. Therefore, a kind of trade-off is required. In practice a number between 4 and 8 images has proved to be sufficient for achieving the goal in less than one second. Nevertheless, despite of having a quite large number of input images, the required time still less than 1 second for generating the maps and less than 2.5 seconds for segmenting them.

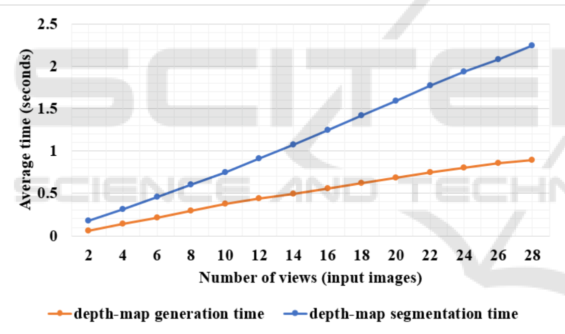

Figure 11: Average time required to generate and segment depth-maps, corresponding to a given number of views.

Finally, to estimate performance of the time required for the detection and classification of the problematic regions, we conducted an experiment using a set of models containing several problematic regions with different sizes. The average problematic region detection time we got is 0.0026 second and the average classification times we got using the statistical and depth classifiers are 0.042 and 0.80 second respectively.

5 CONCLUSION AND FUTURE WORK

A simple approach for the detection and classification of holes in point sets is proposed. In this research, it has been proved that depth-map is a robust and efficient resource for the detection of problematic regions in point-clouds. We also proved that simple statistical measures can be used for the automatic classification of the detected problematic regions in point sets. The results of the experiments we got are quite promising. Holes are accurately identified and classified. Nevertheless, there are still some problems that need to be addressed in future. For example, robustness to lighting variations on surfaces, as well as to noise in point clouds. Also, our future work will concentrate in filling holes, which are classified as virtual holes.

ACKNOWLEDGMENTS

The authors would like to thank the German Academic Exchange Service (DAAD) for providing financial support for research studies. We are grateful to our colleagues who provided insight and expertise that greatly assisted this research work.

REFERENCES

Abdou, I. E. and Pratt, W. K., 1979. Quantitative design and evaluation of enhancement/thresholding edge detectors. *Proceedings of the IEEE*, *67*(5), pp.753-763.

Alismail, H., Browning, B. and Lucey, S., 2016. Direct Visual Odometry using Bit-Planes. *arXiv preprint arXiv:1604.00990*.

Alismail, H., Browning, B. and Lucey, S., 2016. Photometric Bundle Adjustment for Vision-Based SLAM. *arXiv preprint arXiv:1608.02026*.

Bendels, G. H., Schnabel, R. and Klein, R., 2006. Detecting holes in point set surfaces.

Boykov, Y. and Funka-Lea, G., 2006. Graph cuts and efficient ND image segmentation. *International journal of computer vision*, *70*(2), pp.109-131.

Dey, T. K. and Giesen, J., 2003. Detecting undersampling in surface reconstruction. In *Discrete and Computational Geometry* (pp. 329-345).

Furukawa, Y. and Ponce, J., 2010. Accurate, dense, and robust multiview stereopsis. *IEEE transactions on pattern analysis and machine intelligence*, *32*(8), pp.1362-1376.

Haluška, J., 2015. On fields inspired with the polar HSV-RGB theory of Colour. *arXiv preprint arXiv:1512.01440*.

Kong, L. X., Yao, Y. and Hu, Q. X., 2010. Hole boundary identification algorithm for 3D closed triangle mesh. *Computer Engineering*, *36*, pp.177-180.

Lindeberg, T., 2012. Scale invariant feature transform. *Scholarpedia*, *7*(5), p.10491.

Muratov, O., Slynko, Y., Chernov, V., Lyubimtseva, M., Shamsuarov, A. and Bucha, V., 2016. 3DCapture: 3D Reconstruction for a Smartphone. In *Proceedings of the IEEE Conference on Computer Vision and Pattern Recognition Workshops* (pp. 75-82).

Noble, J. A., Gupta, R., Mundy, J., Schmitz, A. and Hartley, R.I., 1998. High precision X-ray stereo for automated 3D CAD-based inspection. *IEEE Transactions on Robotics and automation*, *14*(2), pp.292-302.

Saponaro, P., Sorensen, S., Rhein, S., Mahoney, A.R. and Kambhamettu, C., 2014, October. Reconstruction of textureless regions using structure from motion and image-based interpolation. In *2014 IEEE International Conference on Image Processing (ICIP)* (pp. 1847-1851). IEEE.

Scharstein, D. and Szeliski, R., 2002. A taxonomy and evaluation of dense two-frame stereo correspondence algorithms. *International journal of computer vision*, *47*(1-3), pp.7-42.

Snavely, N., Seitz, S. and Szeliski, R., 2006. Photo Tourism: Exploring Image Collections in 3D. *ACM Transactions on Graphics*.

Snavely, N., Seitz, S. M. and Szeliski, R., 2008. Modeling the world from internet photo collections. *International Journal of Computer Vision*, *80*(2), pp.189-210.

Strecha, C., von Hansen, W., Van Gool, L., Fua, P. and Thoennessen, U., 2008, June. On benchmarking camera calibration and multi-view stereo for high resolution imagery. In *Computer Vision and Pattern Recognition, 2008. CVPR 2008,* pp. 1-8.

Tomasi, C. and Kanade, T., 1992. Shape and motion from image streams under orthography: a factorization method. International Journal of Computer Vision, 9(2), pp.137-154.

Wang, J. and Oliveira, M. M., 2007. Filling holes on locally smooth surfaces reconstructed from point clouds. *Image and Vision Computing*, *25*(1), pp.103-113.

Wang, Y., Liu, R., Li, F., Endo, S., Baba, T. and Uehara, Y., 2012, August. An effective hole detection method for 3D models. In *Signal Processing Conference (EUSIPCO), 2012 Proceedings of the 20th European* (pp. 1940-1944). IEEE.

Wu, C., 2011. VisualSFM: A visual structure from motion system.

Zaman, F., Wong, Y. P. and Ng, B. Y., 2016. Density-based Denoising of Point Cloud. *arXiv preprint arXiv:1602.05312*.